Prediction of high spatio-temporal resolution land surface temperature under cloudy conditions using microwave vegetation index and ANN

CrossMark

H.R. Shwetha [a], D. Nagesh Kumar [a,b,∗]

[a] Department of Civil Engineering, Indian Institute of Science, Bangalore 560012, India
[b] Centre for Earth Sciences, Indian Institute of Science, Bangalore 560012, India

ARTICLE INFO

ABSTRACT

Land Surface Temperature (LST) with high spatio-temporal resolution is in demand for hydrology, climate change, ecology, urban climate and environmental studies, etc. Moderate Resolution Imaging Spectroradiometer (MODIS) is one of the most commonly used sensors owing to its high spatial and temporal availability over the globe, but is incapable of providing LST data under cloudy conditions, resulting in gaps in the data. In contrast, microwave measurements have a capability to penetrate under clouds. The current study proposes a methodology by exploring this property to predict high spatio-temporal resolution LST under cloudy conditions during daytime and nighttime without employing in-situ LST measurements. To achieve this, Artificial Neural Networks (ANNs) based models are employed for different land cover classes, utilizing Microwave Polarization Difference Index (MPDI) at finer resolution with ancillary data. MPDI was derived using resampled (from 0.25° to 1 km) brightness temperatures (T_b) at 36.5 GHz channel of dual polarization from Advance Microwave Scanning Radiometer (AMSR)-Earth Observing System and AMSR2 sensors. The proposed methodology is tested over Cauvery basin in India and the performance of the model is quantitatively evaluated through performance measures such as correlation coefficient (r), Nash Sutcliffe Efficiency (NSE) and Root Mean Square Error (RMSE). Results revealed that during daytime, AMSR-E(AMSR2) derived LST under clear sky conditions corresponds well with MODIS LST resulting in values of r ranging from 0.76(0.78) to 0.90(0.96), RMSE from 1.76(1.86) K to 4.34(4.00) K and NSE from 0.58(0.61) to 0.81(0.90) for different land cover classes. During nighttime, r values ranged from 0.76(0.56) to 0.87(0.90), RMSE from 1.71(1.70) K to 2.43(2.12) K and NSE from 0.43 (0.28) to 0.80(0.81) for different land cover classes. RMSE values found between predicted LST and MODIS LST during daytime under clear sky conditions were within acceptable limits. Under cloudy conditions, results of microwave derived LST were evaluated with air temperature (T_a) and indicate that the approach performed well with RMSE values lesser than the results obtained under clear sky conditions for land cover classes for both day and nighttimes.

1. Introduction

Land Surface Temperature (LST) is the radiative skin temperature of the uppermost part of the earth's surface. It is a primary element in the fields of climate change, hydrology, energy balance models, vegetation monitoring urban climate and environmental studies because it represents integrated features of land atmosphere physical and dynamic processes (Choi et al., 2009; Jin, 2000; Wang and Dickinson, 2012; Li et al., 2013). Due to its rapid variations in both temporal and spatial scales, ground 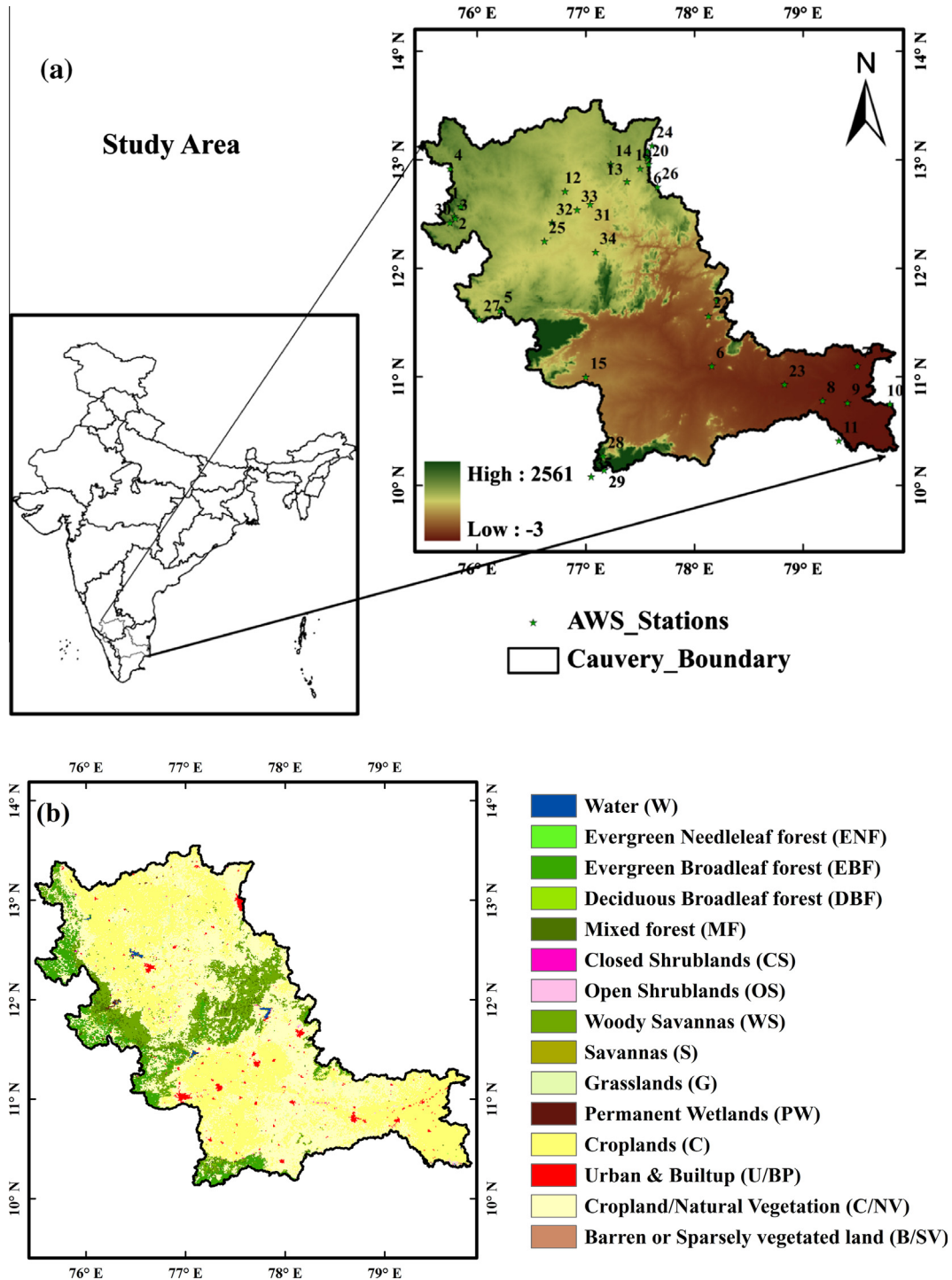based observations of LST over large areas have become inept. With an advancement of remote sensing techniques, LST observations from the satellite data have emerged as the only viable way to provide data of high spatial and temporal resolutions over the entire globe. Mostly LST measurements are retrieved from the thermal infrared bands of sensors such as Moderate Resolution Imaging Spectroradiometer (MODIS), Advanced Very High Resolution Radiometer (AVHRR), Enhanced Thematic Mapper plus (ETM+) etc. In the past few decades, researchers have developed generalized split window algorithm, day and night algorithm or three channel LST algorithms to estimate LST (Li et al., 2013; Pandya et al., 2014). However, these sensors are strongly influenced by cloud, atmospheric water content and aerosols and hence fail to provide data under these scenarios.

∗ Corresponding author at: Centre for Earth Sciences, Indian Institute of Science, Bangalore 560012, India. Fax: +91 80 2360 0404.
E-mail address: nagesh@civil.iisc.ernet.in (D.N. Kumar).

This results in paucity of LST data for many applications. Usually, 50% of the earth surface is covered by clouds at any time which significantly modifies the surface energy budget (Jin, 2000; Kustas and Norman, 1996). Normally, LST forms an integral part in the methods to estimate sensible, latent heat fluxes and soil moisture; hence it is essential to estimate LST even under overcast conditions. Researchers have attempted to derive high spatio-temporal resolution of LST under cloudy conditions using infrared sensors. Jin and Dickinson (2000) proposed the methodology to estimate LST under

cloudy pixels using neighboring clear pixels with the surface energy balance equation based physical algorithm. This approach may not work in the case of difficulty in finding any neighbor clear pixel spatially and temporally. Lu et al. (2011) developed a methodology to retrieve LST under clouds from Meteosat Second Generation/ Scanning-Enhanced Visible and Infrared Imager (MSG/SEVIRI) using temporal neighboring-pixel approach. This approach can be applicable only to daytime measurements. Hengl et al. (2012) predicted spatio-temporal daily temperatures using MODIS LST images
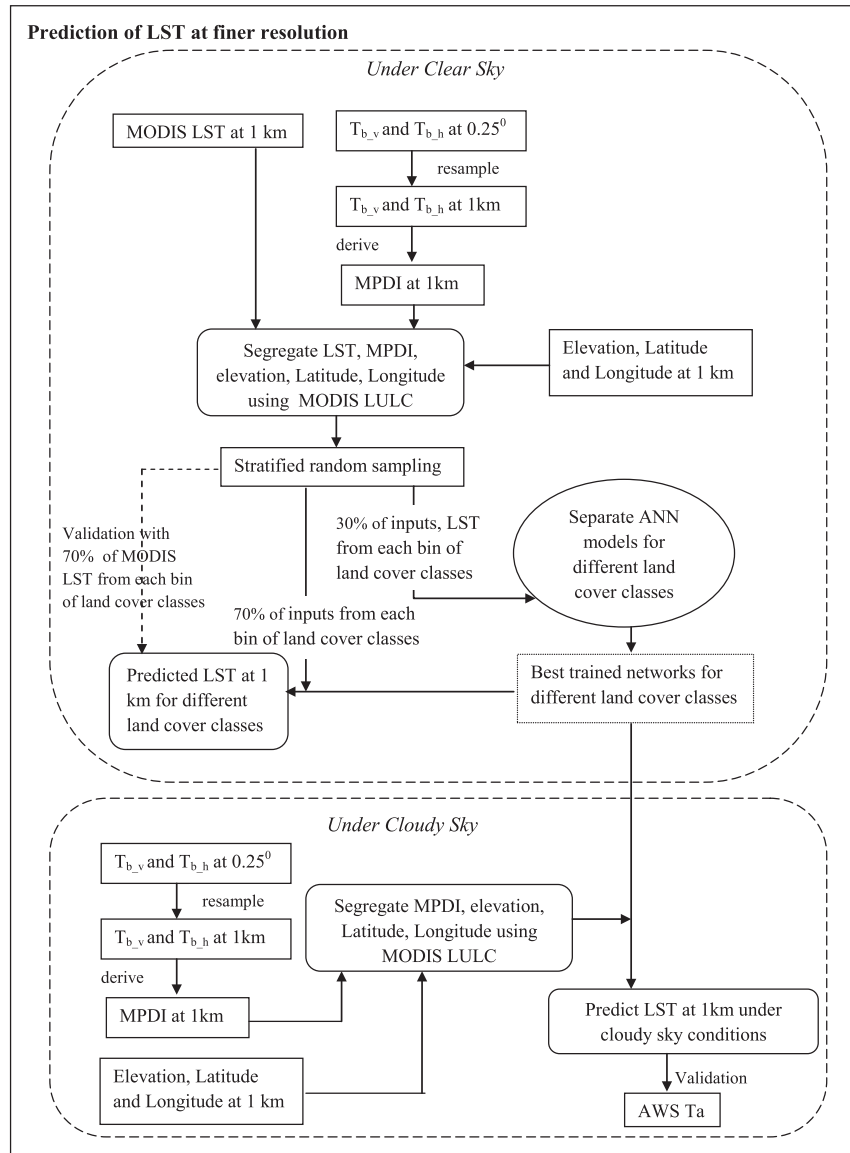

Fig. 1. (a) Location of the study area along with elevation changes. Automatic weather stations and its land cover types indicated by numbers (Station ID 1–3 belong to EBF, station ID 4–5 belong to WS, station ID 6–14 belong to C, station ID 15–18 belong to U & BP and station ID 19–35 belong to C & NV land cover classes) and (b) land cover classes in the study area.

Table 1
Details about the data set used in this study.

Source	Parameter	Product name	Spatial resolution	Purpose
MODIS/Aqua	LST	MYD11A1	1 km	Prediction of LST
AMSR-E/Aqua	T_b at 36.5 GHz, v and h polarizations	L3	0.25°	Derivation of MPDI (Prediction of LST)
AMSR2/GCOM-W	T_b at 36.5 GHz, v and h polarizations	L3	0.25°	Derivation of MPDI (Prediction of LST)
MODIS/Aqua	LULC	MCD12Q1	500 m	Prediction of LST
SRTM	Elevation	–	90 m	Prediction of LST
AWS	T_a	–	Point scale	Validation

Where, v = vertical polarization, v = horizontal polarization, LULC = land use land cover

Fig. 2. Flowchart depicting methodology.

combined with ground measurements of temperatures along with topographic predictors using geostatistical methods. In their study, additional ground based measurements were required but these are very difficult to be obtained especially in the developing countries like India and not easy to measure even in the developed countries. In this regard, LST measurements from the microwave radiometers can complement the available LST measurements from infrared sensors.

Microwave radiations can penetrate through non precipitating clouds and are less effected by atmospheric absorption and by water vapor and therefore these can provide LST data under nearly all sky conditions (Basist et al., 1997). Researchers have successfully derived LST from the microwave measurements from regional to global scale. Owe and Van de Griend (2001) established a relationship between thermodynamic surface temperature and brightness temperature (T_b) at 37 GHz of vertical polarization channel to
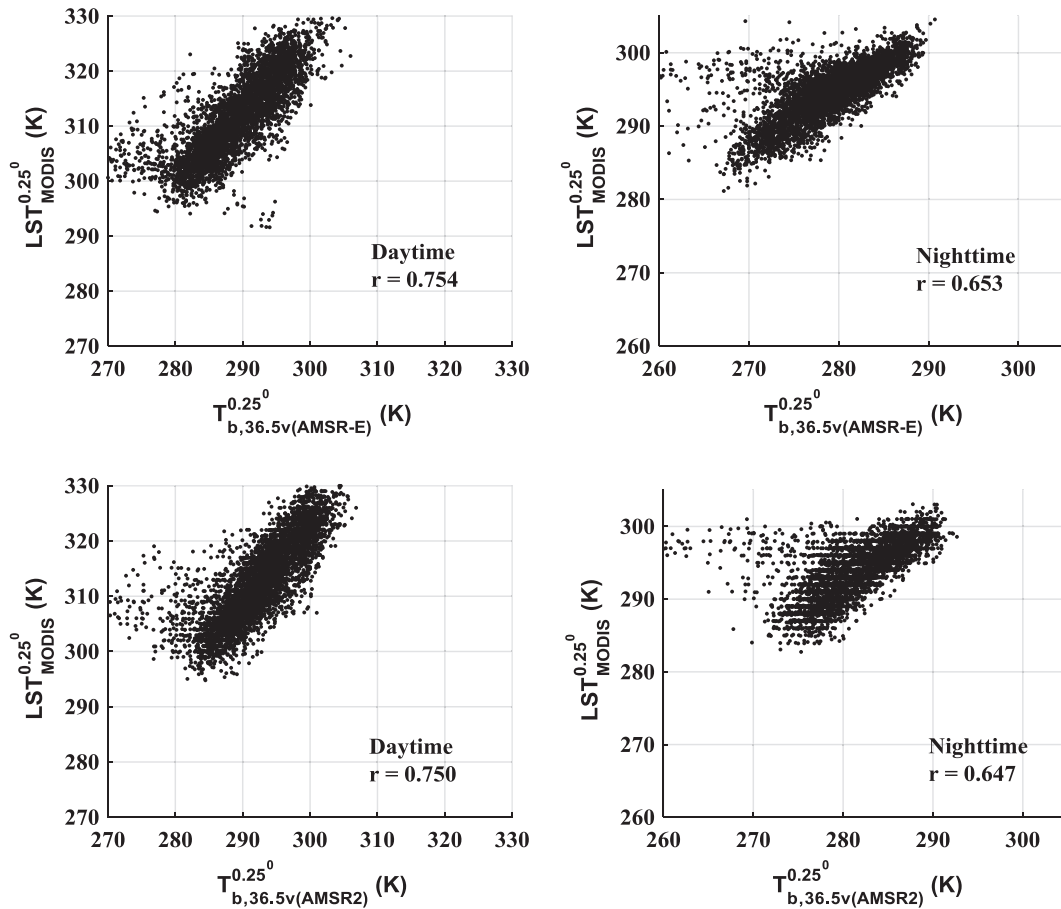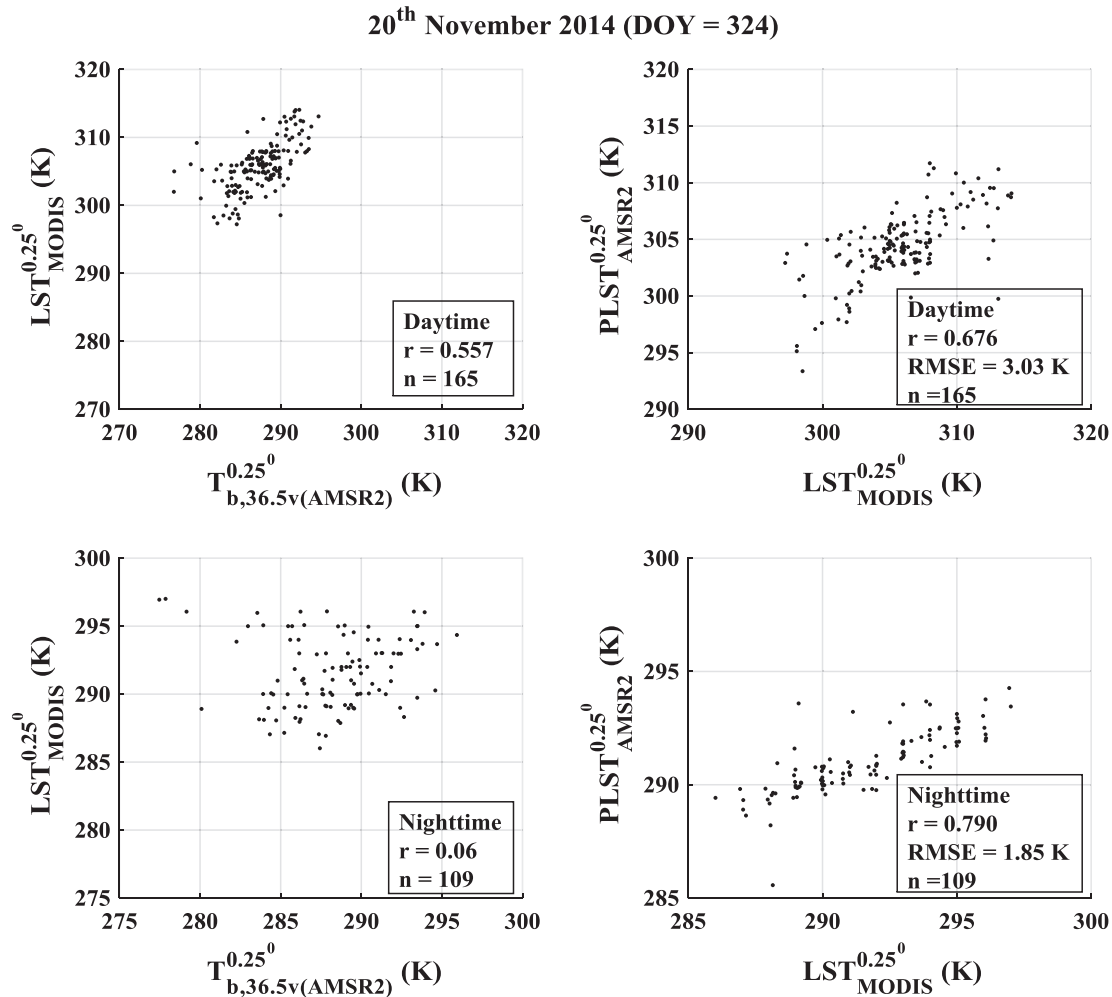
Fig. 3. Scatter plots between $T_{b,v}$ at 36.5 GHz channel and MODIS LST at 0.25° resolution.

estimate LST under semi-arid conditions. Aires et al. (2001) used neural network approach including first guess for the retrieval of LST and other geophysical parameters from special sensor microwave imager (SSM/I) observations over the globe. Fily et al. (2003) found strong linear relationship between microwave surface emissivities of 19 GHz and 37 GHz channels at vertical and horizontal polarizations and these relationships were used in the radiative transfer equation to derive LST over sub-arctic areas. Aires et al. (2004) developed temporal interpolation algorithm to reconstruct LST diurnal cycle over the globe from few LST measurements based on principle component analysis (PCA) /iterative approach under clear and cloudy conditions. Gao et al. (2008) developed a methodology to estimate LST over Amazonian forest by establishing a relationship between polarization ratios and surface emissivity. Holmes et al. (2009) examined the possibility of utilizing 37 GHz to derive LST globally. Chen et al. (2011) proposed a simplified LST regression model for five land cover types based on Microwave Polarization Difference Index (MPDI), combining LST observations from meteorological stations with Advanced Microwave Scanning Radiometer-EOS (AMSR-E) T_b at different frequency channels. However, the predicted LST from microwave observations under cloudy conditions are of coarse resolution, which constrains their application in regional studies. Several studies have focused on disaggregation of coarse resolution LST of thermal bands to fine resolution. Most of these have used high spatial auxiliary data with low temporal resolutions such as NDVI, soil moisture content, vegetation water content, emissivity, reflectance from visible and infrared bands to obtain LST at high spatio-temporal resolutions by establishing linear or nonlinear relationships between them (Deng and Changshan, 2013;

Rodriguez-Galiano et al., 2012; Huang et al., 2013; Zaksek and Ostir, 2012; Keramitsoglou et al., 2013; Yang et al., 2010; Zhan et al., 2013). Recently, some researchers have predicted high spatio-temporal LST by fusing LST from different sensors (Gao et al., 2006; Weng et al., 2014; Wu et al., 2015). However, all these studies have successfully fused LST of the thermal sensors under clear sky conditions to obtain high spatio-temporal LST. To the best of our knowledge, prediction of LST from the microwave measurements at finer resolution under cloudy conditions has not been attempted in the past. So there is a dire necessity of a methodology to estimate subpixel LST under cloudy conditions.

Although several researchers have used T_b from 37 GHz channel and multifrequency channels or by in-situ measurements to derive LST using statistical methods over different parts of the world, application of microwave measurements to derive LST are seldom available for India. Therefore, the present study attempts to develop a methodology to predict high spatio-temporal LST under both clear and cloudy conditions without utilizing in-situ LST measurements. To accomplish this objective, a simple procedure is developed. This includes, derivation of MPDI from the resampled T_bs of dual polarizations from 0.25° to 1 km using cubic convolution method. Secondly, establishment of nonlinear relationship between MODIS LST at 1 km (LST_{MODIS}^{1km}) and MPDI with auxiliary dataset under clear sky conditions for different land cover classes using ANN based models. Finally, to predict LST at high spatial resolution under cloudy conditions by employing relationship obtained under clear sky conditions with an assumption that the relationship obtained under clear sky conditions is also valid under cloudy sky conditions. Predicted LST obtained under clear conditions are further validated with LST_{MODIS}^{1km} and air temperature (T_a),

20th November 2014 (DOY = 324)

Fig. 4. Scatter plots between $LST_{MODIS}^{0.25°}$ (day/night) and $PLST_{AMSR2}^{0.25°}$ (day/night), $T_{b,v(AMSR2)}^{0.25°}$ for 20th November of the year 2014.

whereas under cloudy conditions these are evaluated by comparing only with T_a due to unavailability of LST_{MODIS}^{1km}. The proposed methodology is applied to both day and night images and also the potentiality of this methodology is examined by employing AMSR-E and AMSR2 data.

2. Study area and data used

2.1. Study area

For the current study, Cauvery river basin in India (Fig. 1) has been selected as the study area, which extends from 10°05′ N to 13°30′ N latitude and 75°30′ E to 79°45′ E longitude. It covers an area of 81,155 km² and lies in the States of Karnataka, Kerala, Tamil Nadu and Pondicherry of India. Cauvery basin experiences a tropical climate. The recorded maximum and minimum air temperatures are 44 °C and 18 °C respectively. Physiographically, the basin can be divided into three parts: the Western Ghats area, the Plateau of Mysore and the Delta area (http://india-wris.nrsc.gov.in/wrpinfo/title=Cauvery). The delta area is the most fertile tract in the basin. Western Ghats are mountainous region, which run parallel to the western coast of the Indian peninsula. These are indicated in green color in Fig. 1(b). Major parts of the basin are covered by croplands. The main crops grown in this basin are paddy, sugarcane, ragi and jowar, in addition coffee, pepper, banana, betel vine, gingili, onion, cotton, black gram are also grown. Forest covers 19.53% of the total basin (www.indiawaterportal.org). Uppermost part of

the river basin (Karnataka, Kerala) receives rainfall during south-west monsoon (June–September), whereas, lower part of the basin (Tamil Nadu, Pondicherry) receives rainfall during north-east monsoon (October–January).

2.2. Data sets

MODIS and AMSR-E are sensors carried on National Aeronautics and Space Administration (NASA)'s polar orbiting Aqua satellite since 2002, which passes from south to north at about 1:30 AM/PM local solar time in each day in sun synchronous orbit. MODIS sensor, with 36 bands, provides near-daily global coverage with high spatial resolution. AMSR-E is a dual polarized passive microwave radiometer, operating at 6.9, 10.7, 18.7, 23.8, 36.6 and 89.0 GHz. It was turned off on 4th of October 2011 and its successor AMSR2 on Global Change Observation Mission-Water (GCOM-W) started functioning from July 2012. It has similar characteristics of AMSR-E, with higher spatial resolution. In the present study, daily global 0.25° grids (L3) of T_b at 36.5 GHz channel of AMSR-E and AMSR2 are considered for the years 2010 and 2014 respectively. MODIS LULC (MCD12Q1) is used for segregating the LST pixels according to the International Geosphere Biosphere Programme (IGBP) classification. Digital elevation data is obtained from Shuttle Radar Topography Mission (SRTM). Since the passing time of the satellite over the study region is in the afternoon, maximum LST can be seen during this time and minimum LST occurs in the early morning. The difference between minimum LST and observed LST
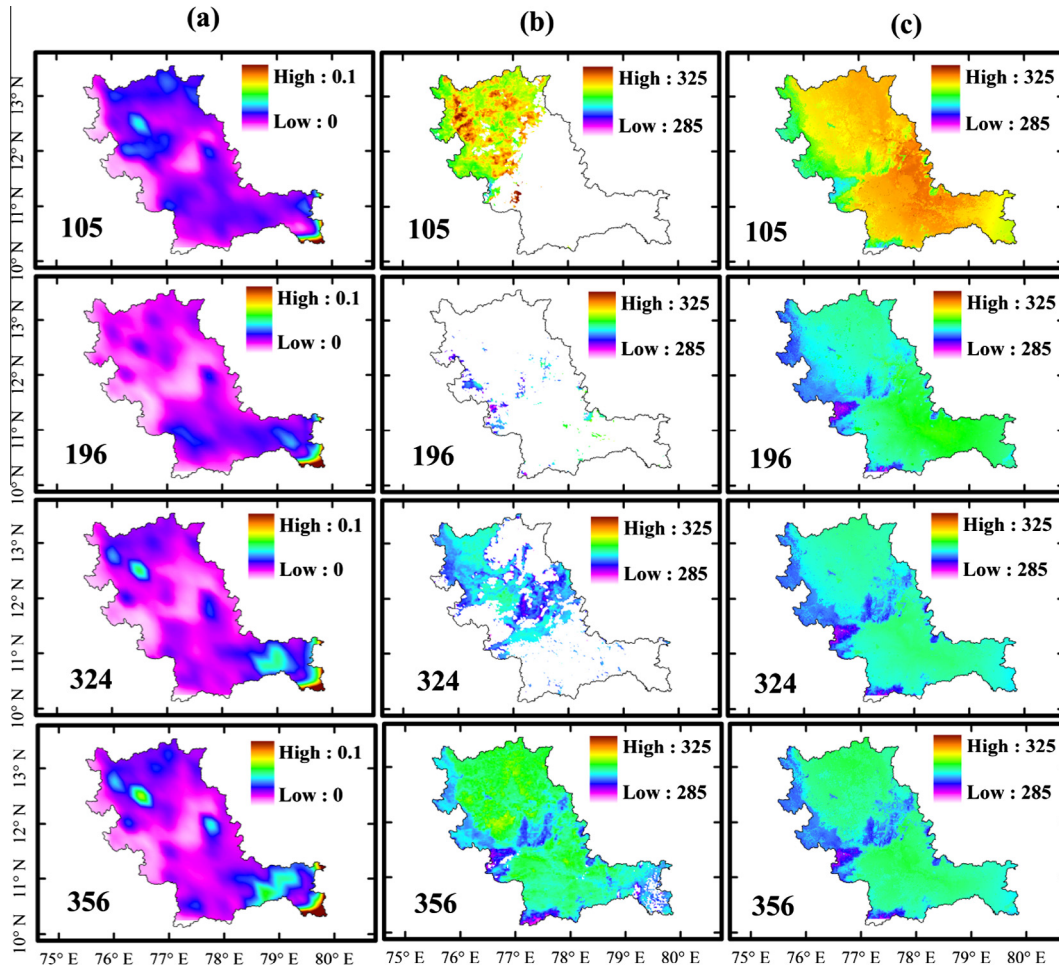
Fig. 5. Spatial variations of (a) $MPDI^{1km}_{AMSR-E}$, (b) LST^{1km}_{MODIS} (K), (c) $PLST^{1km}_{AMSR-E}$ (K) for daytime of 105th, 196th, 324th and 356th days of the year 2010, representing different seasons.

at around 2 am is less; hence in this study nighttime LST refers to minimum LST and daytime LST to maximum LST with the corresponding T_a measurements. Automatic Weather Station (AWS) provide hourly T_a measurements and these were set up by Indian Space Research Organization (ISRO). Details about the dataset used are provided in Table 1.

3. Methodology

3.1. Data processing

T_b of dual polarized at 36.5 GHz channel of level3 daily global 0.25° gridded datasets of AMSR-E and AMSR2 are chosen for the study. Since all datasets have to be consistent with each other, MODIS products sinusoidal projection are changed to AMSR-E and AMSR2 geographical projection by nearest neighbor method using MODIS reprojection tool developed by NASA. For the prediction of LST under cloudy conditions, T_bs are resampled from 0.25° resolutions to the MODIS spatial resolution of 1 km by cubic convolution method. Later, MODIS LULC and SRTM elevation are also upscaled from 500 m and 90 m to 1 km respectively, these products are utilized as an auxiliary data in an ANN model (Detail of this technique is given in the subsequent sections).

3.2. Prediction of LST under cloudy conditions at fine spatial resolution

Vegetation influences the derivation of LST from the satellite measurements. Biophysical properties of vegetation effect its

own thermal response (Quattrochi and Ridd, 1998). MPDI is a good indicator of biophysical properties and represents the density of the land surface vegetation cover. It is also sensitive to vegetation water content (Becker and Choudhury, 1988; Chen et al., 2011; Paloscia and Pampaloni, 1988, 1992). It can be expressed as

$$MPDI_s = \frac{T_{b,v} - T_{b,h}}{0.5 * (T_{b,v} + T_{b,h})} \tag{1}$$

where $T_{b,v}$ and $T_{b,h}$ denotes brightness temperature at vertical (v) and horizontal (h) polarizations respectively and the subscript 's' indicates AMSR-E or AMSR2 sensors derived product. Over vegetated surface, the difference between $T_{b,v} - T_{b,h}$ diminishes until it reaches $T_{b,v} \approx T_{b,h}$ for a dense forest. For bare soil, large polarization difference exists (Han et al., 2015). In this study, $MPDI_s$ represents the daily physical variability which is strongly influenced by soil moisture and vegetation, surface roughness over bare soil and vegetation surface respectively. In this study, $T_{b,v}$ and $T_{b,h}$ are resampled from 0.25° to 1 km using cubic convolution method and these were used to derive MPDI at 1 km resolution ($MPDI^{1km}_s$). Along with this four other constant physical parameters such as elevation, latitude, longitude and Julian day are employed as inputs to the feed-forward ANN model, to predict LST under cloudy conditions at finer resolution, since these geographical and topographical parameters also influence the LST (Hais and Kucera, 2009). The purpose of this model is to assess the nonlinear relationship between input and output variables for both day and night, expressed in the form of
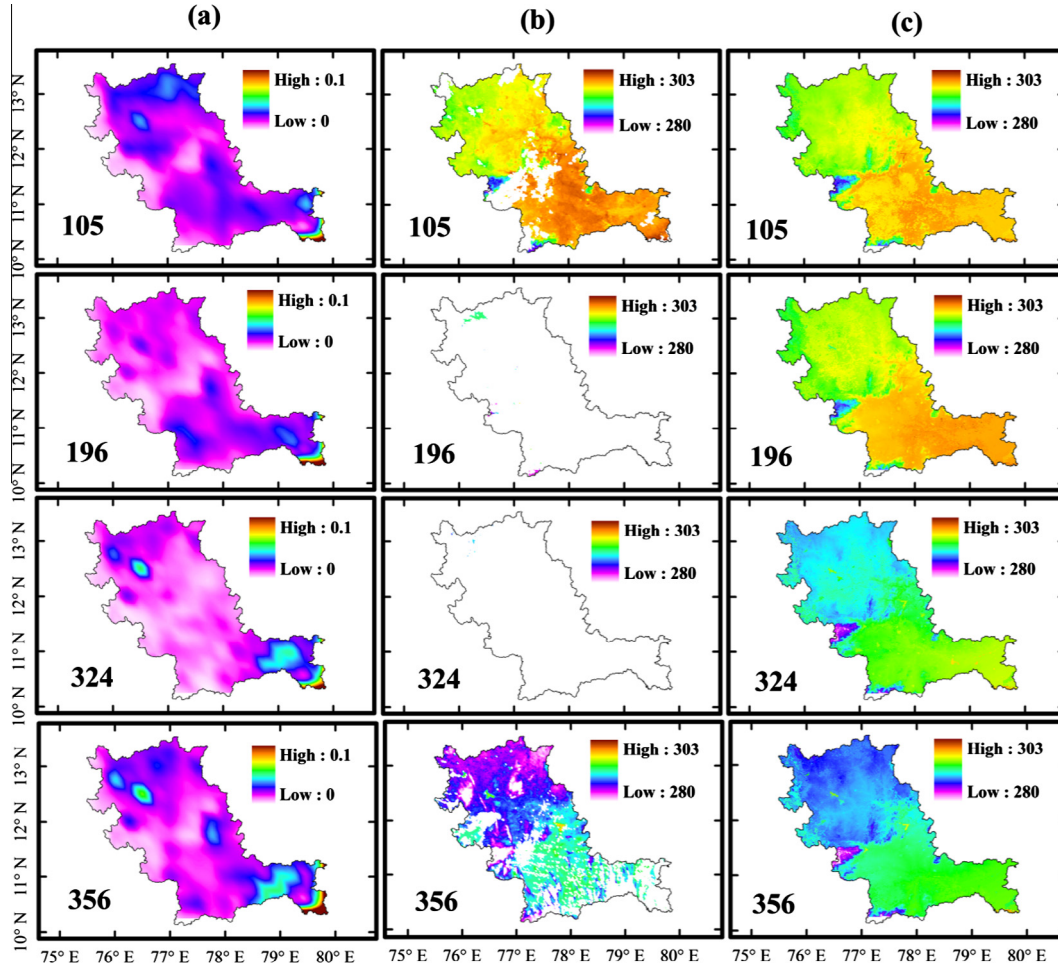
Fig. 6. Spatial variations of (a) $MPDI_{AMSR-E}^{1km}$, (b) LST_{MODIS}^{1km} (K), (c) $PLST_{AMSR-E}^{1km}$ (K) for nighttime of 105th, 196th, 324th and 356th days of the year 2010, representing different seasons.

$$LST_{ij_{MODIS}}^{1km} \ (\text{day/night}) = f(MPDI_{ij_s}^{1km} \ (\text{day/night}), \ elevation_i,$$
$$latitude_i, \ longitude_i, \ Julian \ day) \tag{2}$$

where LST_{MODIS}^{1km} is the MODIS LST at 1 km resolution of the pixel i on the day j. $MPDI_s^{1km}$ is the MPDI at 1 km resolution of the pixel i on the day j for AMSR-E and AMSR2 sensors. The five inputs are incorporated into the model to get relationship with the corresponding LST_{MODIS}^{1km} in the training process. Before beginning the process, input variables are selected based on LST_{MODIS}^{1km} availability (selected for clear sky conditions). The procedure for the prediction of LST at finer resolution ($PLST_s^{1km}$) under cloudy conditions is as follows: (1) Resample (coarse (0.25°) to fine spatial resolution (1 km)) the $T_{b,36.5v(s)}^{0.25°}$ and $T_{b,36.5h(s)}^{0.25°}$ obtained from the microwave measurements. (2) Derive MPDI at 1 km spatial resolution ($MPDI_s^{1km}$) from resampled $T_{b,(s)}$s using an Eq. (1). (3) Segregate the derived $MPDI_s^{1km}$, elevation, latitude, longitude (inputs) and LST_{MODIS}^{1km} (output) of clear and cloudy sky conditions pixels using MODIS LULC data. (4) Under clear sky conditions, using stratified random sampling divide the inputs and output data (into 10 bins). (5) Select 30% of inputs and output data from each bin and relate the $MPDI_s^{1km}$ and other auxiliary data to LST_{MODIS}^{1km} under clear sky condition using ANN approach (for training and testing) and remaining 70% inputs and output data used for validation. (6) Derive high spatial resolution LST ($PLST_s^{1km}$) under cloudy conditions from $MPDI_s^{1km}$

with auxiliary data (available at cloudy pixels) using the trained relationships obtained for the clear pixels. Perform the steps (4–6) for all the land cover classes separately, to derive $PLST_s^{1km}$ under cloudy sky conditions.

Stratified random sampling technique is employed to select data for training an ANN model. For this, LST data are arranged in ascending order and corresponding to this, other inputs are selected. The datasets are divided into 10 bins and from each bin 30% of data are randomly chosen for training and testing the network and remaining 70% data are used for validation. For training the data, feed-forward neural networks are employed with five algorithms namely sequence of Levenberg Marquardt, resilient back propagation, scaled conjugate gradient algorithm, Broyden, Fletcher, Goldfarb and Shanno (BFGS) quasi Newton algorithm, and a conjugate gradient algorithm with Fletcher Reeve restarts (Canelon and Chavez, 2011; Hagan and Menhaj, 1994; Mas and Flores, 2008; Roberts et al., 2010). In this process each node of ANN output variable is simulated by iterative adjustment and optimizing of the connection weights and threshold values, so that the simulated values become equal or close to the targets (ASCE, 2000). Trial and error process is applied to select the optimal architecture. The best network is selected based on Pearson correlation coefficient (r), Nash Sutcliffe Efficiency (NSE) and Root Mean Square Error (RMSE) performance measures. Further, to predict LST under cloudy conditions, all five inputs (present in the cloudy conditions) are applied in the selected best network with an assumption that
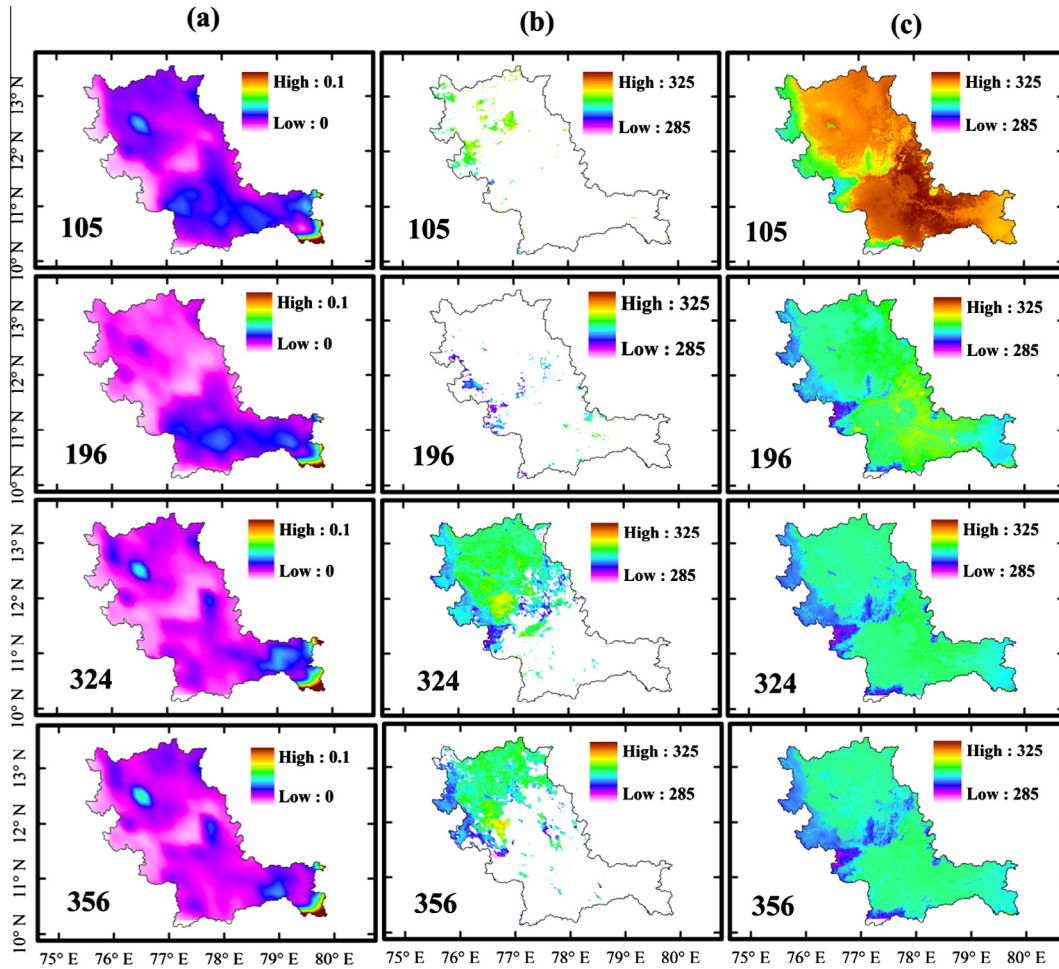
Fig. 7. Spatial variations of (a) $MPDI_{AMSR-2}^{1km}$, (b) LST_{MODIS}^{1km} (K), (c) $PLST_{AMSR-2}^{1km}$ (K) for daytime of 105th, 196th, 324th and 356th days of the year 2014, representing different seasons.

the relationship between LST and the five inputs under clear pixels holds good even for the cloudy pixels as well. This procedure is followed to predict both day and night LST ($PLST_s^{1km}$) under clear and cloudy conditions for both the sensors. The overall methodology used in this study is shown in Fig. 2. r, NSE and RMSE are used to quantify the error between LST_{MODIS}^{1km} (day/night) and $PLST_s^{1km}$ (day/night) under clear sky conditions, whereas under cloudy conditions $PLST_s^{1km}$ (day/night) are evaluated with the corresponding T_a (day/night). In literature, researchers had established a strong relationship between T_a and LST under clear and cloudy conditions and also suggested a procedure to evaluate microwave derived LST with T_a under cloudy conditions (Catherinot et al., 2011; Gallo et al., 2011; Gao et al., 2008; Jin et al., 1997; Mildrexler et al., 2011; Prigent et al., 2003; Schwarz et al., 2012). These enabled us to validate microwave derived LST (day/night) products with the corresponding T_a (day/night) available from Automatic Weather Stations (AWS) under cloudy conditions in this study. T_a data quality control checks are also conducted as suggested by Allen (2008).
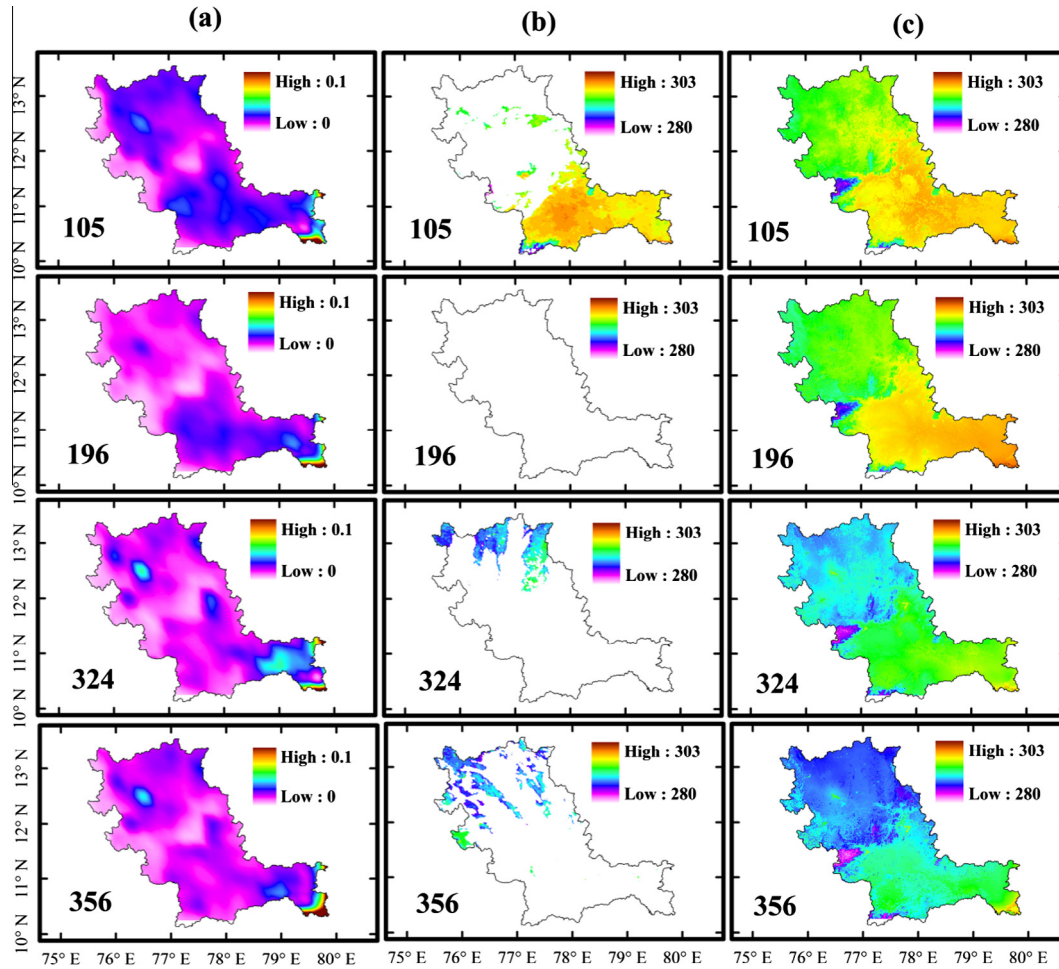
4. Results and discussion

Initially, the linear relationships between $T_{b,v}$ at 36.5 GHz of AMSR-E ($T_{b,36.5v(AMSR-E)}^{0.25°}$), AMSR2 ($T_{b,36.5v(AMSR2)}^{0.25°}$) sensors and $LST_{MODIS}^{0.25°}$ for daytime and nighttime are established for the study region (Fig. 3). $T_{b,v}$ at 36.5 GHz channel of both sensors are selected because of their frequent usage for the LST retrieval in literature (Fily et al., 2003; Holmes et al., 2009). r values of 0.754 and 0.750 for daytime, whereas for nighttime 0.653 and 0.647 are obtained for AMSR-E and AMSR2 sensors respectively. Since MPDI is sensitive to vegetation water content and can represents vegetation density, surface roughness and these parameters strongly effect LST variation, hence it has been utilized to predict LST under cloudy conditions.

Spatial variations of $MPDI_S^{1km}$ for the days of the year (105th, 196th, 324th, and 356th) representing four seasons (summer, rainy, post monsoon and winter) are shown in Figs. 5(a)–8(a). During daytime lower $MPDI_S^{1km}$ was found in the forest regions for all the seasons, whereas for croplands slightly higher values were obtained. In the summer season (105th, day of the year) higher $MPDI_S^{1km}$ values were found in the croplands than other seasons for both the sensors. During rainy season lower $MPDI_S^{1km}$ value corresponds to the upper part of the basin, this is because upper part of the basin receives rainfall during this time. Lower MPDI values shifted to lower part of the region, since lower part of the basin gets rainfall during October to January (324th and 356th days of the year) as shown in Figs. 5(a) and 7(a). Similar variations could be seen during nighttime for both sensors derived $MPDI_S^{1km}$.

Furthermore to check the potentiality of an ANN model, 20th November 2014 (day of the year = 324th) data has been removed from the dataset. Remaining $MPDI_{AMSR2}^{0.25°}$ with ancillary datasets

Fig. 8. Spatial variations of (a) $MPDI_{AMSR-2}^{1km}$, (b) LST_{MODIS}^{1km} (K), (c) $PLST_{AMSR-2}^{1km}$ (K) for nighttime of 105th, 196th, 324th and 356th days of the year 2014, representing different seasons.

are incorporated into the ANN model to derive the nonlinear relationship with the corresponding pixels of $LST_{MODIS}^{0.25°}$ under clear sky conditions. Subsequently, the best trained network is selected based on the r, RMSE and NSE evaluation measures and this network is further used to derive $PLST_{AMSR2}^{0.25°}$ under clear and cloudy conditions. $PLST_{AMSR2}^{0.25°}$ (day/night) under clear sky conditions validated against $LST_{MODIS}^{0.25°}$ (day/night) using statistical error indices (Fig. 4). As indicated by the statistical error indices, the results show the prediction accuracy yielded r values 0.676 and 0.790 and RMSE values 3.03 K and 1.85 K for daytime and nighttime respectively. The linear relationships between $T_{b,36.5v(AMSR2)}^{0.25°}$ and $LST_{MODIS}^{0.25°}$ were examined for day and nighttimes, results in very low r values of 0.06 for nighttime and 0.557 for daytime. This indicates that the proposed model has shown better performance by implementing MPDI instead of $T_{b,v}$.

4.1. Evaluation of predicted LST at finer resolution

ANN models are applied separately for different land cover classes to estimate $PLST_s^{1km}$ (day/night) under cloudy conditions. To achieve this, $T_{b,36.5v(s)}^{0.25°}$ and $T_{b,36.5h(s)}^{0.25°}$ (day/night) obtained from the microwave measurements are resampled from 0.25° to 1 km using cubic interpolation method. Derived $MPDI_s^{1km}$ (day/night) from resampled T_bs of dual polarizations with other auxiliary products are employed in an ANN model to obtain nonlinear

relationship with LST_{MODIS}^{1km} (day/night) under clear sky conditions for different land cover classes. These relationships are used under cloudy conditions to predict $PLST_s^{1km}$ (day/night) using available inputs data. The accuracy of the proposed methodology is evaluated using LST_{MODIS}^{1km} (day/night) and T_a (day/night). $PLST_s^{1km}$ (day/night) obtained under clear sky conditions are compared with the LST_{MODIS}^{1km} (day/night) and T_a (day/night). Whereas, $PLST_s^{1km}$ (day/night) obtained under cloudy conditions are compared only with the T_a (day/night), since LST under cloudy conditions were not available from the thermal infrared sensors.

4.1.1. Evaluation of predicted LST with MODIS LST under clear sky conditions

Spatial variations of LST_{MODIS}^{1km} and $PLST_s^{1km}$ for days of the year (105th, 196th, 324th, 356th) representing the four seasons namely summer, rainy, post monsoon and winter respectively are shown in Figs. 5(b) and (c)–8(b) and (c) for daytime and nighttime. Spatial variations of LST_{MODIS}^{1km} and $PLST_s^{1km}$ obtained from the AMSR-E (2010) and AMSR-2 (2014) sensors data are shown in Figs. 5 and 6 and Figs 7 and 8 respectively. As the figures indicate, spatio-temporal patterns of $PLST_s^{1km}$ (day/night) for the four seasons have similar variations like LST_{MODIS}^{1km} (day/night) at clear pixels for different land cover classes by initial visual interpretation. Cloudy pixels present in the LST_{MODIS}^{1km} (day/night) were masked according to the information provided in the quality assessment (QA) layer and
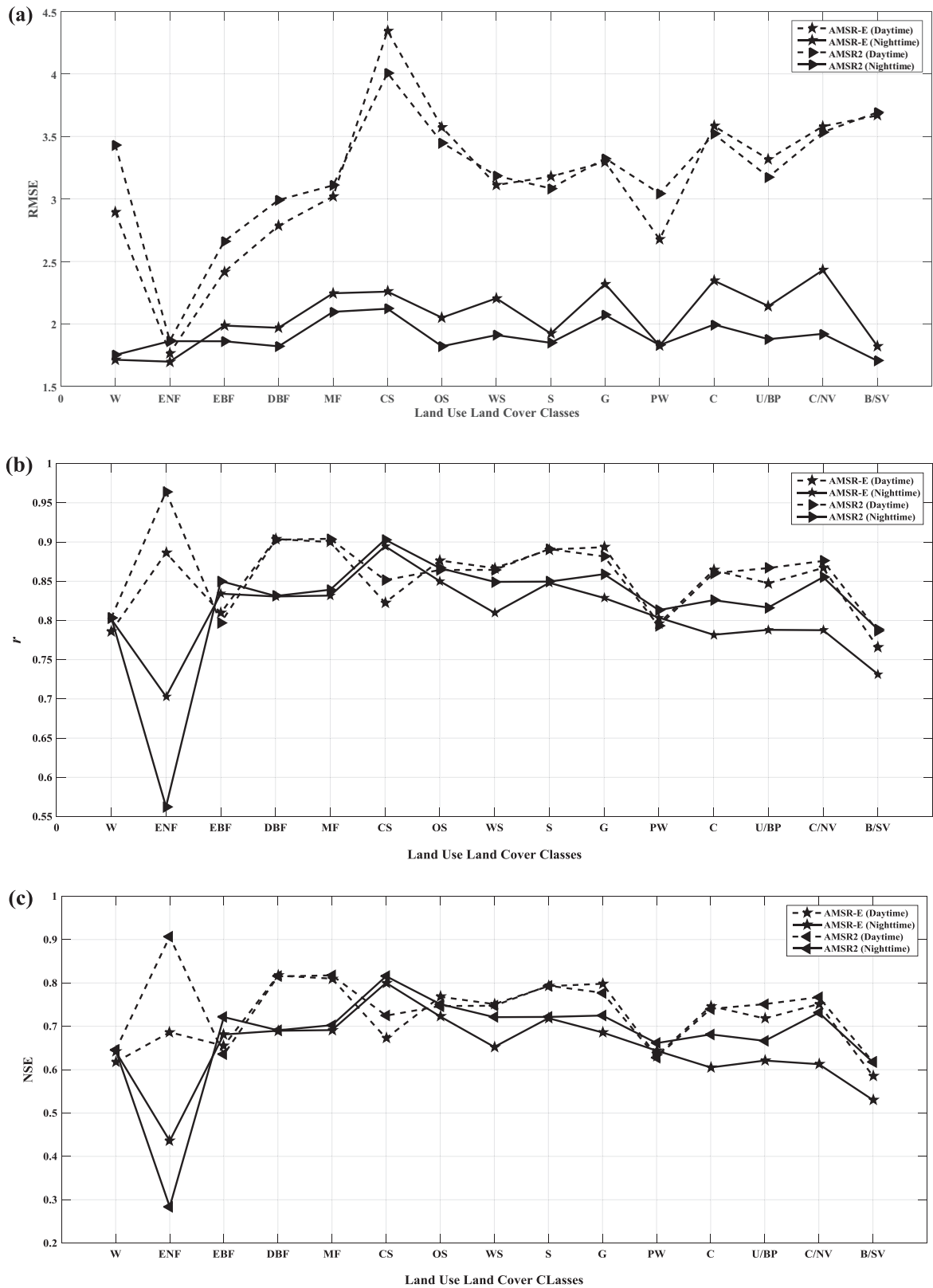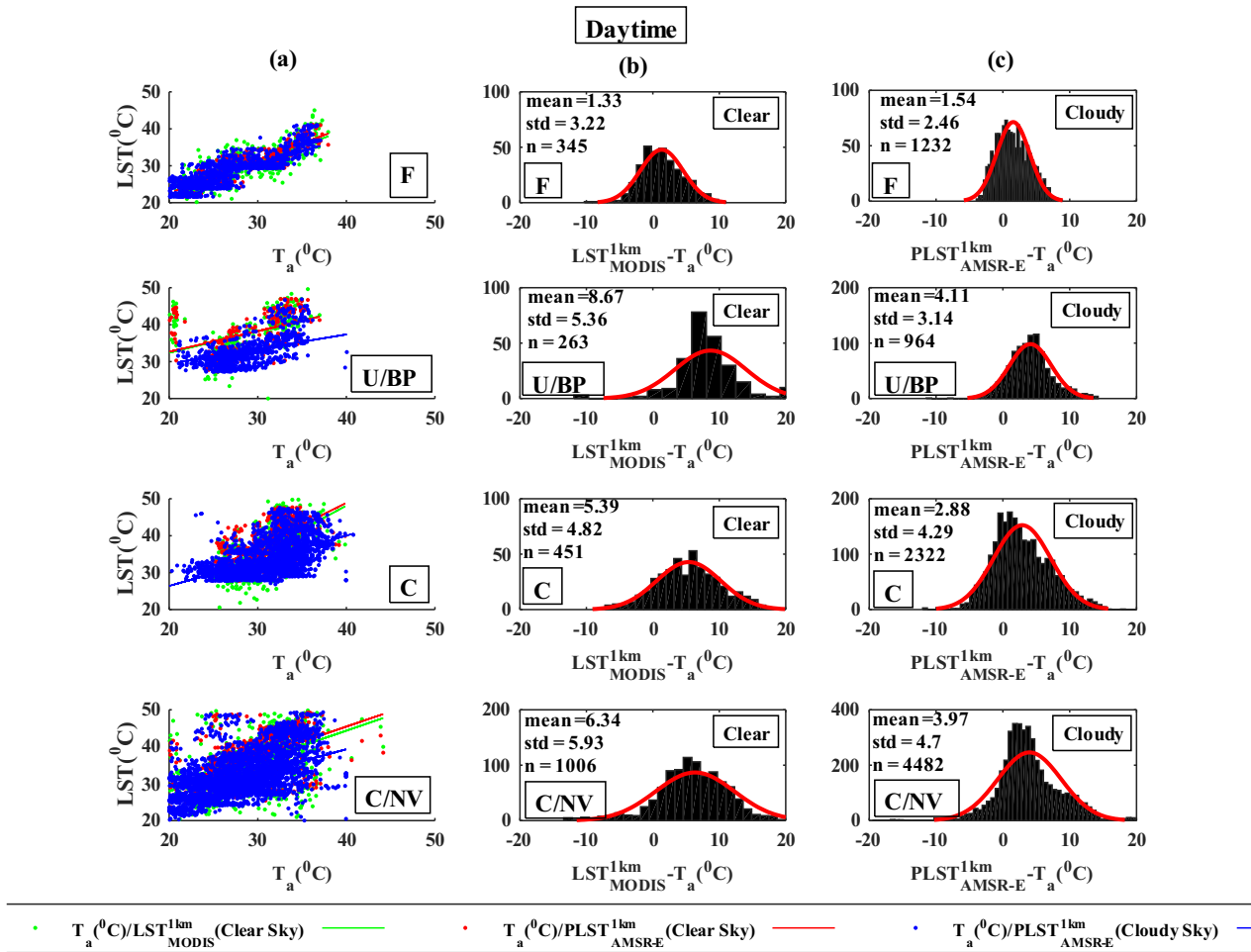
Fig. 9. (a) RMSE, (b) r, (c) NSE values calculated by evaluating $PLST_s^{1km}$ with LST_{MODIS}^{1km} for different land cover classes.

represented in white color in the study region (Figs. 5(b)–8(b)). During daytime, LST_{MODIS}^{1km}, $PLST_s^{1km}$ in the Western Ghats have less values compared to other regions of the study area, because these regions are covered with dense forests. Croplands and Cropland/

Natural vegetation dominates the other classes in the basin and showed higher $PLST_s^{1km}$ values. For summer season $PLST_s^{1km}$ and LST_{MODIS}^{1km} values are found to have higher values in the basin than the other seasons. During nighttime, $PLST_s^{1km}$ corresponds to

Fig. 10. (a) Scatter plots between T_a and LST_{MODIS}^{1km}, $PLST_{AMSR-E}^{1km}$ under clear and cloudy conditions, (b) histograms of the difference between LST_{MODIS}^{1km} and T_a, (c) histograms of the difference between $PLST_{AMSR-E}^{1km}$ and T_a during daytime for different land cover classes.
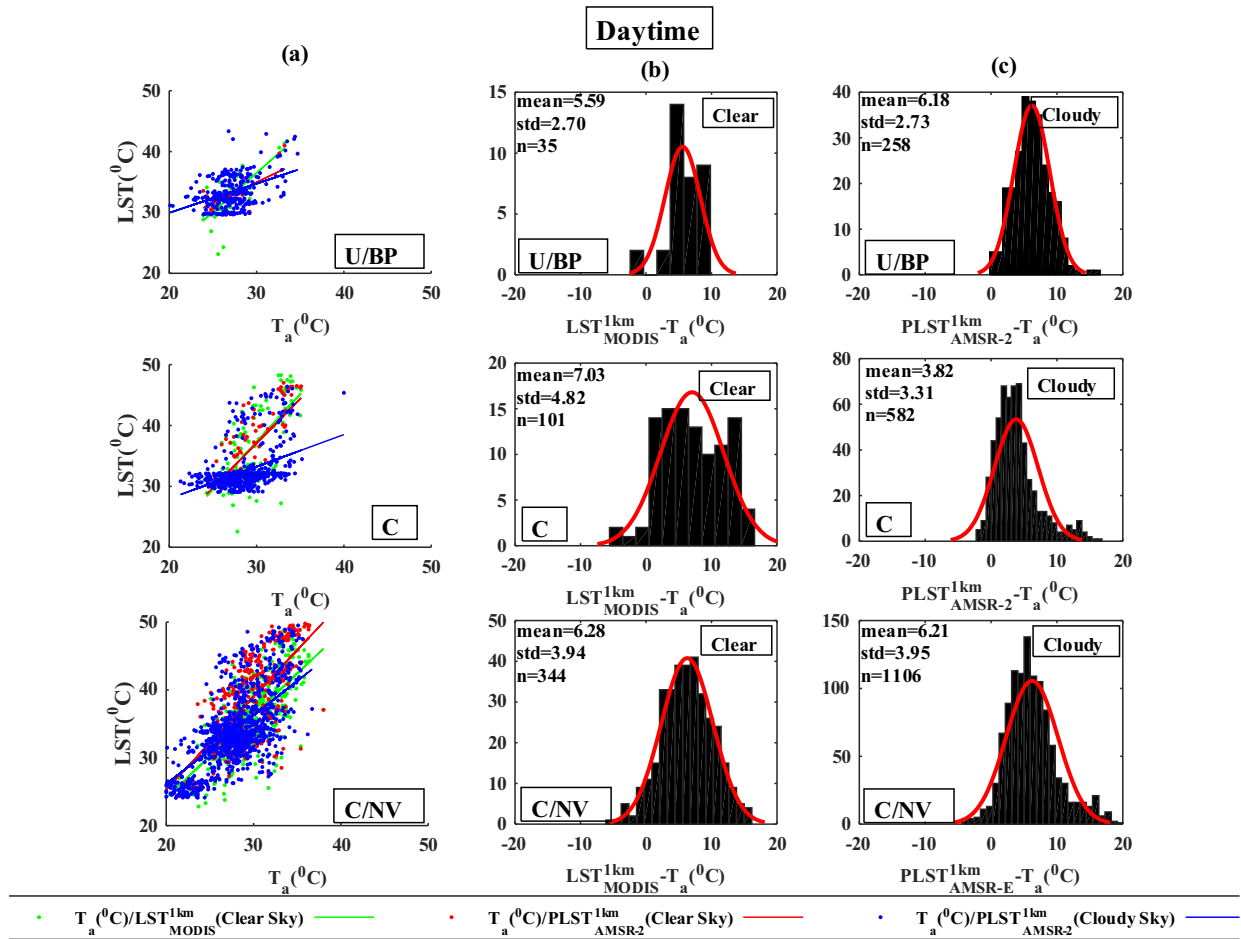
LST_{MODIS}^{1km} at all land cover classes, but with lower LST values. Forest region has lesser LST values compared to other classes of the basin. Lower LST values can be discerned in the upper part of the basin for all the seasons and this is due to higher elevation. During nighttime LST drops due to radiative cooling, which depends on the elevation, presence of clouds and relative humidity. Seasonal variations of $PLST_s^{1km}$ are perfectly captured well with LST_{MODIS}^{1km} for both day and nighttimes indicating better performance of the ANN approach and during winter season both have lower values than other seasons for upper and lower parts of the basin.

Furthermore, to quantify the prediction efficiency of the ANN model, as mentioned in Section 3.2, 70 percent data of the clear sky pixels from each bin for different land cover classes are considered to compute r, RMSE and NSE. Fig. 9 presents the results obtained between LST_{MODIS}^{1km} and $PLST_s^{1km}$ by these standard statistical performance measures for different land cover classes. Out of the five algorithms used in feed forward neural network, Levenberg Marquardt algorithm performed well. Overall, correlation coefficients for different land covers for AMSR-E (AMSR2) have ranged from 0.76(0.78) to 0.90(0.96) for daytime and 0.70(0.56) to 0.89(0.90) for nighttime images at clear pixels. RMSE values computed between $PLST_s^{1km}$ and LST_{MODIS}^{1km} are within the limits as found in the literature, for both sensors (Fily et al., 2003; Holmes et al., 2009) for all the land cover classes for both day and night. NSE values ranged between 0.58(0.61) to 0.81(0.90) for daytime and 0.43(0.28) to 0.80(0.81) for the nighttime observations. The

proposed methodology showed better performance for the grasslands and closed shrubland during daytime and nighttime respectively at the clear pixels. This indicates that $MPDI_s$ for the lower vegetation performed well as inferred in the study of Chen et al. (2011). Surprisingly, evergreen needle leaf forest class during nighttime has yielded less r and NSE values than the other forest regions. As expected for water and barren land, the model has underperformed showing less r and NSE values than the other land cover classes as presented in Fig. 9 for both day and nighttimes. According to IGBP classification, the barren land or sparsely vegetated surface represents the land covered with exposed soil, sand, rocks or snow with never more than 10% vegetation cover during any time of the year. The estimated accuracy is low for this class, because $MPDI_s$ at 36.5 GHz is sensitive to vegetation parameters. Influence of soil parameters become stronger than vegetation parameters in barren land or sparsely vegetated surface. Although $MPDI_s$ has higher values for bare soil, easily distinguishable from other land cover classes, r values are greater than 0.7 in all the cases for both the sensors except for evergreen broadleaf forest (EBF) for nighttime.

4.1.2. Evaluation of predicted LST with surface air temperatures

$PLST_s^{1km}$ (day/night) under clear and cloudy conditions are compared with the corresponding T_a (day/night) available from AWS stations for different land cover classes (Figs. 10–13). T_a (day/night) represents the thermodynamic temperature of the air measured
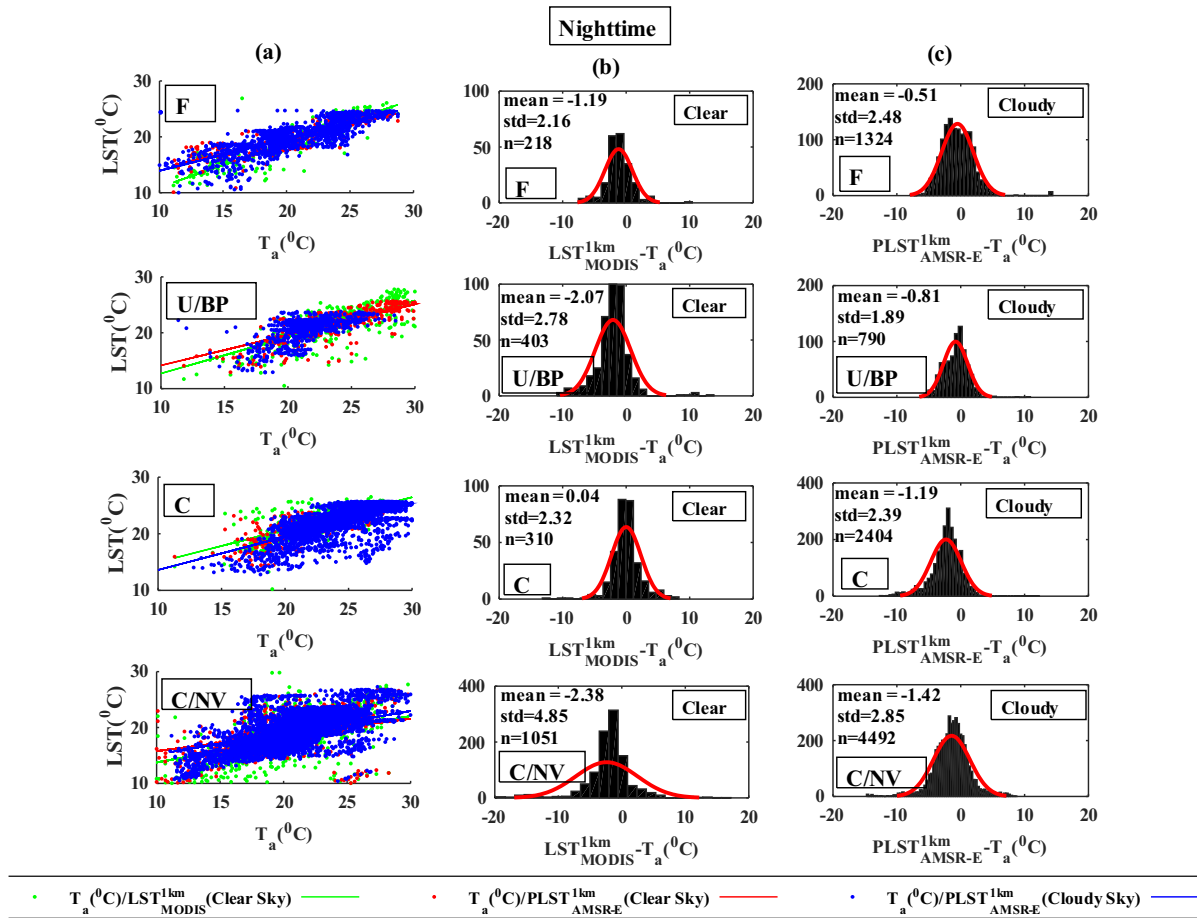
Fig. 11. (a) Scatter plots between T_a and LST_{MODIS}^{1km}, $PLST_{AMSR2}^{1km}$ under clear and cloudy conditions, (b) histograms of the difference between LST_{MODIS}^{1km} and T_a, (c) histograms of the difference between $PLST_{AMSR2}^{1km}$ and T_a during daytime for different land cover classes.

between 1.5 and 3.5 m above the surface. T_a (day/night) differs from the LST (day/night) in physical representations and also differ the most at smaller spatial and temporal scales (Prigent et al., 2003). In this study, the procedure introduced by Prigent et al. (2003) and Catherinot et al. (2011) is followed to compare $PLST_s^{1km}$ (day/night) under cloudy condition with T_a (day/night). AWS stations are available for evergreen broadleaf forest (EBF), woody savannas (WS), croplands (C), built up (U/BP) and cropland/natural vegetation (C/NV) land cover classes. The number of observations present in the EBF and WS classes was less; hence these observations are combined as forest (F) class. Separate analysis has been done for AMSR-E and AMSR2 derived LST. Table 2 and Figs. 10(a)–13(a) present r and RMSE values obtained and scatter plots between LST_{MODIS}^{1km} (day/night) under clear sky, $PLST_s^{1km}$ (day/night) under clear and cloudy sky conditions and corresponding T_a (day/night) respectively. For daytime, under clear sky conditions for AMSR-E sensor, r varied from 0.456 (U/BP) to 0.877 (F) between $PLST_{AMSR-E}^{1km}$ and T_a and 0.436 (U/BP) to 0.756 (F) between LST_{MODIS}^{1km} and T_a. This indicates that the predicted LST correlated better with the corresponding T_a values than the LST_{MODIS}^{1km}. For the cloudy pixels r ranged from 0.514 (C) and 0.855 (F) and r value found less for 'C' class than the clear sky conditions. For AMSR2 sensor, due to paucity of observations for 'F' land cover class, analysis was performed only for U/BP, C and C/NV classes. For daytime r values obtained for these classes were similar to AMSR-E sensor as presented in Table 2 and Fig. 11(a). Usually, during daytime LST is greater than T_a

causing positive difference, which is due to the warming up of surface more quickly during the daytime. Few T_a observations obtained from the AWS stations were slightly higher than the $PLST_{AMSR-E}^{1km}$ under cloudy conditions during daytime and after removal of these observations r values increased for all land cover classes as shown in Fig. 14. This may be due to the presence of standing water. Most of the observations were seen in the rainy and post monsoon seasons. Hence in these scenarios it is advisable to evaluate LST with the in-situ LST measurements. For the AMSR2 sensor very less number of observations, where T_a is greater than $PLST_{AMSR-E}^{1km}$ were found, this results in less improvement in the r values after removing the observations (Fig. 14). During nighttime, similar results were observed (Figs. 12(a) and 13(a)) and r values for all land cover classes were within the limit except for U/BP class. LST cools quickly than T_a at night and has lesser value than T_a. Correlations between $PLST_{AMSR-E}^{1km}$ and T_a were found lesser than the correlations between LST_{MODIS}^{1km} and T_a for the U/BP cover class under cloudy conditions for both sensors. For AMSR2 sensor, r value was greater for cloudy conditions than clear sky conditions for 'C' class during nighttime. The r values found to be significant ($p < 0.05$) for both day and night under clear and cloudy conditions for both sensors.

In addition, RMSE values were computed for both clear and cloudy conditions (Table 2). For daytime, RMSE values ranged from 3.481 (°C) (F) to 10.198 (°C) (U/BP) between LST_{MODIS}^{1km} and T_a under clear conditions whereas, for cloudy pixels minimum of 2.903 (°C)

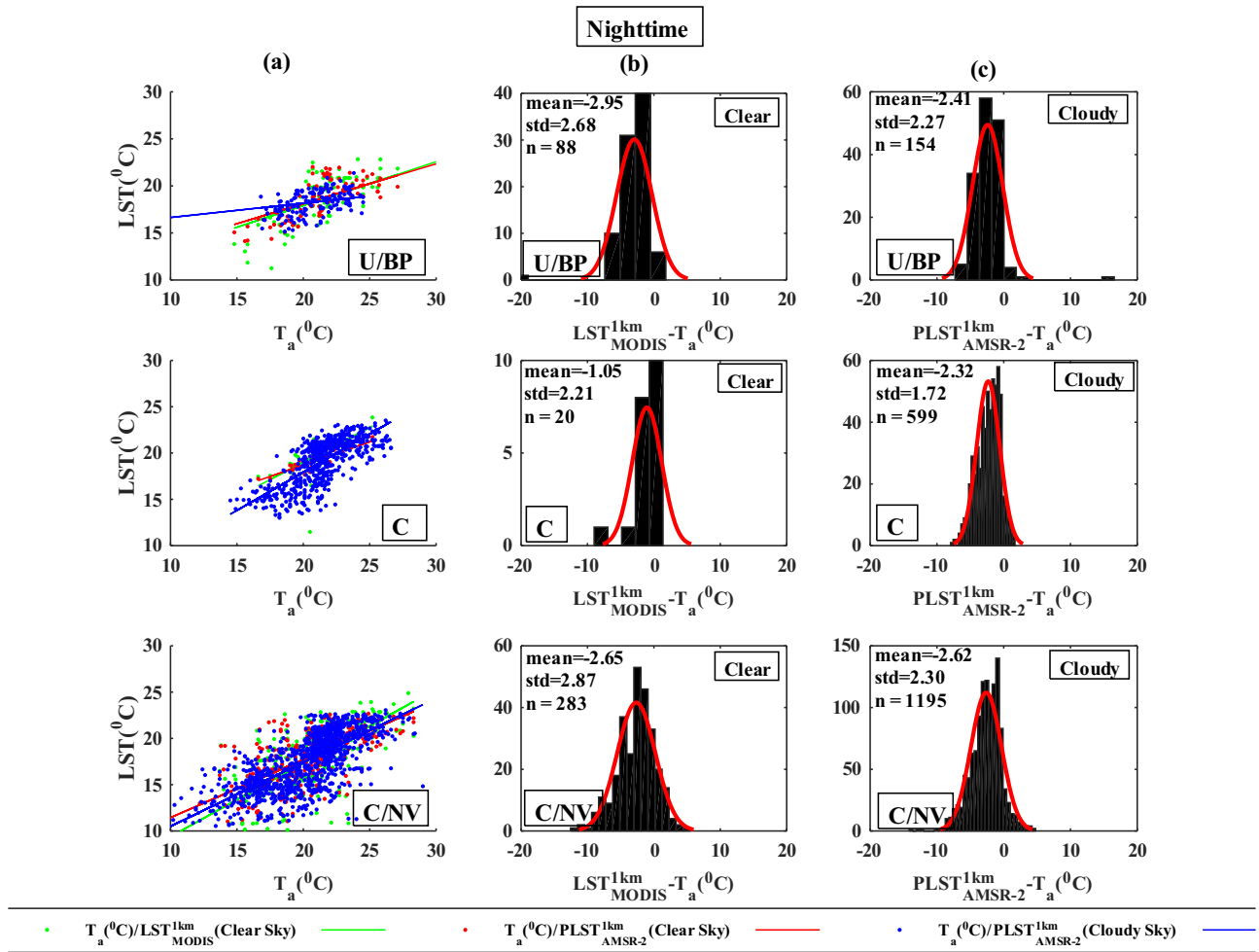**Fig. 12.** (a) Scatter plots between T_a and LST_{MODIS}^{1km}, $PLST_{AMSR-E}^{1km}$ under clear and cloudy conditions, (b) histograms of the difference between LST_{MODIS}^{1km} and T_a, (c) histograms of the difference between $PLST_{AMSR-E}^{1km}$ and T_a during nighttime for different land cover classes.

(F) and maximum of 6.202 (°C) (C/NV) were obtained between $PLST_{AMSR-E}^{1km}$ and T_a for AMSR-E sensor. For the year 2014, RMSE values found varied from 6.194 (°C) (U/BP) to 8.514 (°C) (C) between LST_{MODIS}^{1km} and T_a under clear conditions whereas, at cloudy pixels minimum of 5.063 (°C) (C) and maximum of 7.363 (°C) (C/NV) were obtained. RMSE values for cloudy conditions were found lesser than clear sky conditions for most of the considered land cover classes, indicating that the ANN approach has predicted LST well under cloudy conditions using both satellite sensor data. As presented in Table 2, for nighttime RMSE values observed between $PLST_s^{1km}$ and T_a under cloudy conditions were less compared to clear sky condition for few land cover classes. RMSE values were found less for nighttime than for the daytime for the considered land cover classes.

Toward further evaluation of the microwave derived LST at 1 km resolution under cloudy conditions, the mean and standard deviation of the differences between LST_{MODIS}^{1km} (day/night), $PLST_s^{1km}$ (day/night) and T_a (day/night) are examined for the available land cover classes. The differences between LST and T_a are scale dependent. For smaller spatial and temporal scales they differ the most than the larger scales (Jin et al., 1997). Even though the difference varies largely on regional scales, these are related with land type, soil moisture, vegetation cover and cloud cover. In this study, separate analysis has been done for different land cover classes. The differences exhibited between LST and T_a are assumed to be due to cloud cover. Generally, during daytime under clear sky condition large positive LST-T_a difference can be noticed than under the

cloudy conditions. Whereas, during nighttime, for clear sky condition, negative LST-T_a differences are prominent due to rapid cooling of LST at night and for cloudy conditions, because the reduction of outgoing infrared radiation warms the surface, inducing lesser negative LST-T_a difference. In this study, under clear sky conditions, the differences between LST_{MODIS}^{1km} (day/night) and T_a (day/night) and whereas, for cloudy conditions differences between $PLST_s^{1km}$ (day/night) and T_a (day/night) were considered. Histograms of differences between LST_{MODIS}^{1km} (day/night), $PLST_s^{1km}$ (day/night) and T_a (day/night) under clear and cloudy sky conditions for both day and nighttimes for the considered land cover classes are depicted in Figs. 10(b) and (c)–13(b) and (c). During daytime, the mean and standard deviation of the differences were found less for the cloudy sky conditions compared to clear sky conditions for all the land cover classes except for U/BP class of AMSR2 derived LST (Fig. 11(b) and (c)). In contrast to this, during nighttime the mean difference was found more under cloudy conditions than under clear sky conditions for most of the land cover classes. Similar results (combining all land cover classes) were inferred in Prigent et al. (2003). Thus these results show that the proposed methodology performed well under cloudy conditions for all land cover classes during daytime for both sensors data, but for nighttime and especially under sparsely vegetated surfaces, the model has to be tested under different climatic conditions. Moreover, the predicted LST under cloudy conditions has to be validated with in-situ LST measurements.

Fig. 13. (a) Scatter plots between T_a and LST_{MODIS}^{1km}, $PLST_{AMSR2}^{1km}$ under clear and cloudy conditions, (b) histograms of the difference between LST_{MODIS}^{1km} and T_a, (c) histograms of the difference between $PLST_{AMSR2}^{1km}$ and T_a during nighttime for different land cover classes.

Table 2
r and RMSE values obtained by evaluating $PLST_{AMSR-E}^{1km}$ (day/night) and $PLST_{AMSR-2}^{1km}$ (day/night) with T_a (day/night) under clear and cloudy conditions for the considered land use land cover classes.

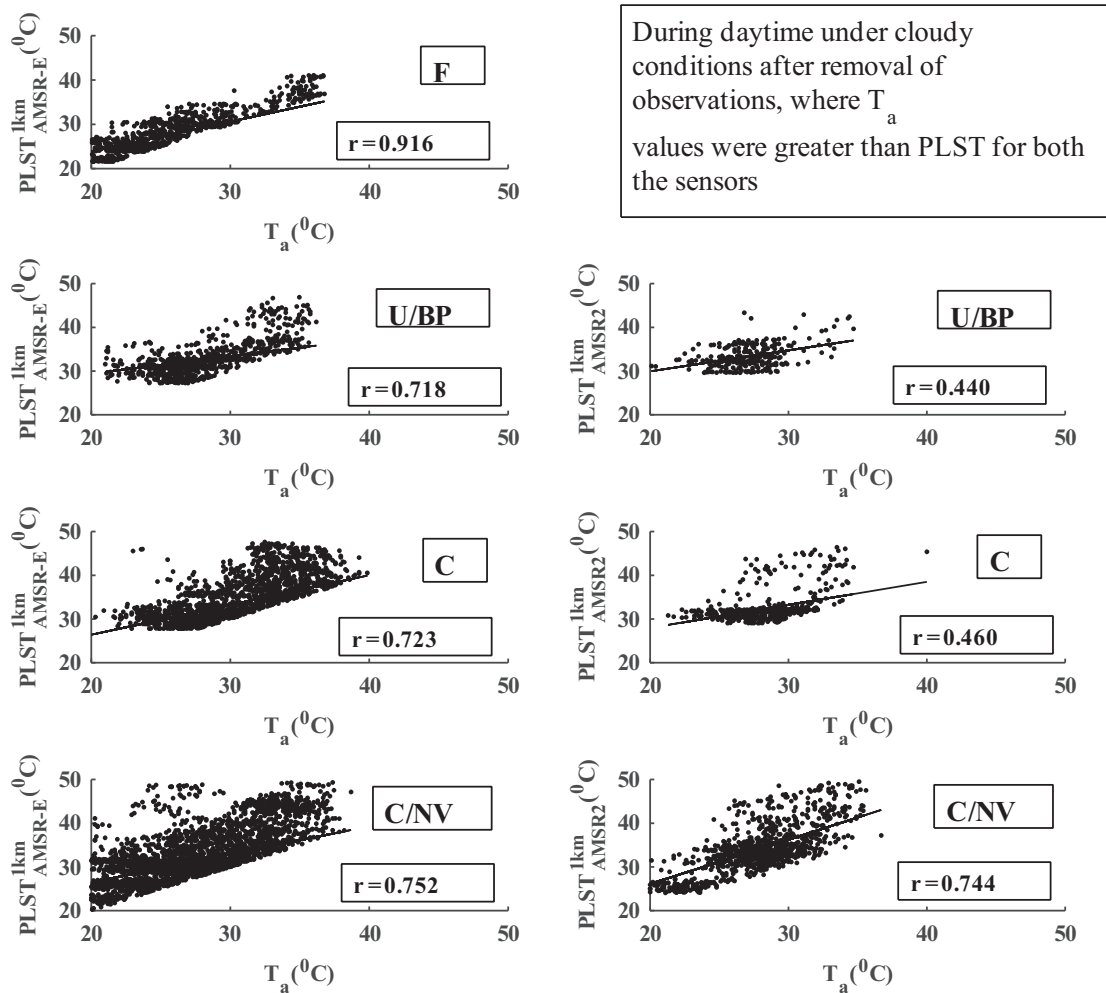| LULC	Under clear sky conditions				Under cloudy sky conditions	
	LST_{MODIS}^{1km}/T_a		$PLST_s^{1km}/T_a$		$PLST_s^{1km}/T_a$	
	R	RMSE	r	RMSE	r	RMSE
During daytime for AMSR-E sensor						
Forest (F)	0.756	3.481	0.877	2.704	0.855	2.903
Urban/Builtup (U/BP)	0.436	10.198	0.456	10.230	0.625	5.176
Croplands (C)	0.620	7.235	0.602	8.436	0.514	5.168
Croplands Natural Vegetation (C/NV)	0.540	8.691	0.564	9.337	0.626	6.202
During nighttime for AMSR-E sensor						
Forest (F)	0.887	2.466	0.861	2.633	0.772	2.536
Urban/Builtup (U/BP)	0.713	3.470	0.791	3.096	0.625	2.063
Croplands (C)	0.682	2.319	0.508	8.673	0.699	3.329
Croplands Natural Vegetation (C/NV)	0.450	5.408	0.381	5.086	0.631	3.194
During daytime for AMSR2 sensor						
Urban/Builtup (U/BP)	0.713	6.194	0.634	6.239	0.424	6.762
Croplands (C)	0.673	8.514	0.710	7.953	0.404	5.063
Croplands Natural Vegetation (C/NV)	0.702	7.416	0.677	10.157	0.705	7.363
During nighttime for AMSR2 sensor						
Urban/Builtup (U/BP)	0.588	3.975	0.653	3.730	0.257	3.316
Croplands (C)	0.534	2.404	0.769	1.824	0.731	2.896
Croplands Natural Vegetation (C/NV)	0.739	3.914	0.733	3.512	0.735	3.487

Fig. 14. Correlation coefficients between T_a and $PLST_{AMSR-E}^{1km}$, $PLST_{AMSR2}^{1km}$ under cloudy conditions for the land cover classes during daytime after removal of observations, where T_a values were greater than LST.

5. Conclusions

The aim of the work was to predict high spatio-temporal resolution of LST under cloudy conditions. To obtain this, initially, brightness temperatures at 36.5 GHz channel of dual polarizations were resampled from coarser to finer spatial resolution. These resampled products were used to derive MPDI at finer spatial resolution. Microwave derived $MPDI_s$ with auxiliary data employed in an ANN model to predict LST at finer spatial resolution under cloudy sky conditions for daytime and nighttime measurements, since thermal infrared sensors are unable to provide LST data under cloudy conditions. To achieve this, MPDIs (day/night) with auxiliary data and corresponding LST_{MODIS}^{1km} (day/night) at clear pixels were employed in ANN model for different land cover classes. Assuming that the best trained network obtained for each land cover class would be equally valid under cloudy conditions, sub-pixel temperatures were estimated using available MPDIs and other auxiliary data at cloudy pixels for each land cover class separately. This procedure was applied for both datasets of AMSR-E and AMSR2 sensors to obtain daily maximum and minimum LST at high spatio-temporal resolution under cloudy conditions.

This study has demonstrated the possibility of combining infrared and passive microwave data to predict LST at high spatio-temporal resolution under cloudy sky conditions. Results revealed good agreement between $PLST_s^{1km}$ (day/night) and

LST_{MODIS}^{1km} (day/night) for day and night images. Estimated $PLST_s^{1km}$ at clear and cloudy pixels were evaluated with LST_{MODIS}^{1km} and T_a. Results from the analysis at clear pixels for all land cover classes showed good correlation between $PLST_s^{1km}$ and LST_{MODIS}^{1km}, T_a for both day and night times. In the absence of in-situ LST measurements under cloudy conditions, predicted LST was evaluated by comparing with T_a (day/night). A reasonable agreement was observed between $PLST_s^{1km}$ (day/night) and T_a (day/night) with lower RMSE values than under the clear sky condition for the considered land cover classes.

The proposed methodology is the most feasible way to predict LST at high spatio-temporal resolution under cloudy conditions in the absence of in-situ LST measurements at all land cover classes during daytime and nighttime. This study has estimated LST for the cloudy pixels using microwave observations at high spatio-temporal resolution and even also for non-vegetated and low vegetation regions under cloudy conditions. The developed model performed well for all land cover classes when compared with LST_{MODIS}^{1km}. However, the applicability of this methodology for the land cover classes such as grasslands and shrublands, where in-situ T_a were unavailable for the study region, needs investigation. Moreover, the methodology necessarily to be validated with in-situ LST measurements under cloudy conditions for all land cover classes, if and when available. Future plan includes facilitating

the usage of the predicted LST at high spatio-temporal resolution under cloudy conditions in the estimation of evapotranspiration and soil moisture over the study region.

References

Aires, F., Prigent, C., Rossow, W.B., Rothstein, M., 2001. A new neural network approach including first guess for retrieval of atmospheric water vapor, cloud liquid water path, surface temperature and emissivities over land from the satellite microwave observations. J. Geophys. Res. 106 (D14), 14887–14907.

Aires, F., Prigent, C., Rossow, W.B., 2004. Temperature interpolation of global surface skin temperature diurnal cycle over land under clear and cloudy conditions. J. Geophys. Res. 108 (D10), 4310.

Allen, R., 2008. Quality assessment of weather data and micrometeological flux – impacts on evapotranspiration calculation. J. Agric. Meteorol. 64 (4), 191–204.

ASCE Task Committee on Application of Artificial Neural Networks in Hydrology (ASCE), 2000. Artificial neural networks in hydrology. II: hydrologic applications. J. Hydrol. Eng. 5 (2), 124–137.

Basist, A., Grody, C.N., Peterson, C.T., Williams, N.C., 1997. Using the Special Sensor Microwave/Imager to monitor land surface temperatures, wetness and snow cover. J. Appl. Meteorol. 37, 888–911.

Becker, F., Choudhury, B.J., 1988. Relative sensitivity of normalized difference vegetation index (NDVI) and microwave polarization difference index (MPDI) for vegetation and desertification monitoring. Remote Sens. Environ. 24, 297–311.

Canelon, Dario J., Chavez, Jose L., 2011. Soil heat flux modeling using artificial neural networks and multispectral airborne remote sensing imagery. Remote Sens. 3, 1627–1643.

Catherinot, J., Prigent, C., Maurer, R., Papa, F., Jimenez, C., Aries, F., Rossow, W.B., 2011. Evaluation of "all weather" microwave-derived land surface temperatures with in situ CEOP measurements. J. Geophys. Res. 116, D23105.

Chen, Shui-sen, Chen, Xiu-zhi, Chen, Wei-qi, Su, Yong-xian, Li, Da, 2011. A simple retrieval method of land surface temperature from AMSR-E passive microwave data – a case study over southern China during the strong snow disaster of 2008. Int. J. Appl. Earth Obs. Geoinf. 13, 140–151.

Choi, Minha, Kustas, William P., Anderson, Martha C., Allen, Richard G., Li, Fuquin, Kjaersgaard, Jeppe H., 2009. An inter comparison of three remote sensing-based surface energy balance algorithms over a corn and soybean production region (Iowa, U.S.) during SMACEX. Agric. For. Meteorol. 149 (12), 2082–2097.

Deng, Chengbin, Wu, Changshan, 2013. Estimating very high resolution urban surface temperature using spectral unmixing and thermal mixing approach. Int. J. Appl. Earth Obs. Geoinformatics 23, 155–164.

Fily, M., Royer, A., Goita, K., Prigent, C., 2003. A simple retrieval method for land surface temperature and fraction of water surface determination from satellite microwave brightness temperatures in sub-arctic areas. Remote Sens. Environ. 85, 328–338.

Gallo, Kevin, Hale, Robert, Tarpley, Dan, Yu, Yunyue, 2011. Evaluation of relationship between air and land surface temperature under clear and cloudy conditions. J. Appl. Meteorol. Climatol. 50, 767–775.

Gao, Feng, Masek, Jeff, Schwaller, Matt, Hall, Forrest, 2006. On the blending of the Landsat and MODIS surface reflectance: predicting daily Landsat surface reflectance. IEEE Trans. Geosci. Remote Sens. 5 (6), 989–993.

Gao, Huilin, Fu, Rong, Dickinson, Robert E., Juarez, Robinson I. Negron, 2008. A practical method for retrieving land surface temperature from AMSR-E over Amazon forest. IEEE Geosci. Remote Sens. 46 (1), 193–199.

Hagan, Martin T., Menhaj, Mohammad B., 1994. Training feedforward neural networks with Marquardt algorithm. IEEE Trans. Geosci. Remote Sens. 26 (5), 617–621.

Hais, Martin, Kucera, Tomas, 2009. The influence of topography on the forest surface temperature retrieved from Landsat TM, ETM+ and ASTER thermal channels. ISPRS J. Photogramm. Remote Sens. 64 (6), 585–591.

Han, Xiao-Jing, Duan, Si-Bo, Tang, Ronglin, Liu, Hai-Qi, Li, Zhao-Liang, 2015. Evaluation of temporal variations in soil moisture based on the microwave polarization difference index using in situ data over agricultural areas in China. Int. J. Remote Sens. RAQRS 4. http://dx.doi.org/10.1080/01431161.2015.1043161.

Hengl, Tomislav, Heuvelink, Gerard B.M., Tadic, Melita Percec, Pebesma, Edzer J., 2012. Spatio-temporal prediction of daily temperatures using time series of MODIS LST images. Theor. Appl. Climatol. 107, 265–277.

Holmes, T.R.H., De Jeu, R.A.M., Owe, M., Dolman, A.J., 2009. Land surface temperature from Ka band (37GHz) passive microwave observations. J. Geophys. Res. 114, D04113.

Huang, Bo, Wang, Juan, Song, Huihui, Fu, Dongjie, Wong, KwanKit, 2013. Generating high spatiotemporal resolution land surface temperature for urban heat island monitoring. IEEE Geosci. Remote Sens. Lett. 10 (5), 1011–1015.

Jin, Menglin, 2000. Interpolation of surface radiative temperature measured from polar orbiting satellites to a diurnal cycle 2. Cloudy-pixel treatment. J. Geophys. Res. 105, 4061–4076.

Jin, Menglin, Dickinson, R.E., 2000. A generalized algorithm for retrieving cloudy sky skin temperature from satellite thermal infrared radiances. J. Geophys. Res. D22, 27037–27047.

Jin, Menglin, Dickinson, R.E., Vogelmann, A.M., 1997. A comparison of CCM2-BATS skin temperature and surface air temperature with satellite and surface observations. J. Clim. 10, 1505–1524.

Keramitsoglou, Iphigenia, Kiranoudis, Chris T., Weng, Qihao, 2013. Downscaling geostationary land surface temperature imagery for urban analysis. IEEE Geosci. Remote Sens. Lett. 10 (5), 1253–1257.

Kustas, W.P., Norman, J.M., 1996. Use of remote sensing for evapotranspiration monitoring over land surfaces. Hydrol. Sci. J. 41 (4), 495–516.

Li, Zhao-Liang, Tang, Bo-Hui, Wu, Hua, Ren, Huazhong, Yan, Guangjian, Wan, Zhengming, Trigo, Isabel F., Sobrino, Jose A., 2013. Satellite-derived land surface temperature: current status and perspectives. Remote Sen. Environ. 131, 14–37.

Lu, L., Venus, V., Skidmore, A., Wang, T., Luo, G., 2011. Estimating land surface temperature under clouds using MSG/SEVIRI observations. Int. J. Appl. Earth Obs. Geoinf. 13, 265–276.

Mas, J.F., Flores, J.J., 2008. The applications of artificial neural networks to the analysis of remotely sensed data. Int. J. Remote Sen. 29 (3), 617–663.

Mildrexler, David J., Zhao, Maosheng, Running, Stevan W., 2011. A global comparison between station air temperatures and MODIS land surface temperatures reveals the cooling role of forests. J. Geophys. Res. 116, G03025.

Owe, M., Van de Griend, A.A., 2001. On the relationship between thermodynamic surface temperature and high frequency (37 GHz) vertically polarized brightness temperature under semi arid conditions. Int. J. Remote Sen. 22 (17), 3521–3532.

Paloscia, S., Pampaloni, S., 1988. Microwave Polarization Index for monitoring vegetation growth. IEEE Trans. Geosci. Remote Sens. 26 (5), 617–621.

Paloscia, S., Pampaloni, S., 1992. Microwave vegetation indexes for detecting biomass and water conditions of agricultural crops. Remote Sen. Environ. 40, 15–26.

Pandya, Mehul R., Shah, Dhiraj B., Trivedi, Himanshu J., Darji, Nikunj P., Ramakrishnan, R., Panigrahy, Sushma, Parihar, Jai Singh, Kirankumar, A.S., 2014. Retrieval of land surface temperature from Kalpana-1 VHRR data using a single-channel algorithm and its validation over western India. ISPRS J. Photogramm. Remote Sens. 94, 160–168.

Prigent, C., Aires, F., Rossow, W.B., 2003. Land surface skin temperatures from a combined analysis of microwave and infrared satellite observations for an all-weather evaluation of the differences between air and skin temperatures. J. Geophys. Res. 108 (D10), 4310.

Quattrochi, D.A., Ridd, M.K., 1998. Analysis of vegetation within a semi-arid urban environment using high spatial resolution airborne thermal infrared remote sensing data. Atmos. Environ. 32, 19–33.

Roberts, J.B., Clayson, C.A., Robertson, F.R., Jackson, D.L., 2010. Predicting near surface atmospheric variables from Special Sensor Microwave/Imager using neural networks with a first guess approach. J. Geophys. Res. 115, D19113.

Rodriguez-Galiano, V., Pardo-Iguzquiza, E., Sanchez-Castillo, M., Chica-Olma, M., Chica-Rivas, M., 2012. Downscaling Landsat 7 ETM+ thermal imagery using land surface temperature and NDVI images. Int. J. Appl. Earth Obs. Geoinformatics 18, 515–527.

Schwarz, Nina, Schlink, Uwe, Franck, Ulrich, GoBmann, Katrin, 2012. Relationship of land surface and air temperatures and its implications for quantifying urban heat island indicators – an application for the city of Leipzig (Germany). Ecol. Ind. 18, 693–704.

Wang, K., Dickinson, R.E., 2012. A review of global terrestrial evapotranspiration: observation, modeling, climatology, and climatic variability. Rev. Geophys. 50, RG2005.

Weng, Qihao, Fu, Peng, Gao, Feng, 2014. Generating daily land surface temperature at Landsat resolution by fusing Landsat and MODIS data. Remote Sen. Environ. 145, 55–67.

Wu, Penghai, Shen, Huanfeng, Zhang, Liangpei, Gottsche, Frank-Michael, 2015. Integrated fusion of multi-scale polar orbiting and geostationary satellite observations for the mapping of high spatial and temporal resolution land surface temperature. Remote Sen. Environ. 156, 169–181.

Yang, Guijan, Pu, Ruiliang, Huang, Wenjiang, Wang, Jihua, Zhao, Chunjiang, 2010. A novel method to estimate subpixel temperature by fusing solar reflective and thermal infrared remote sensing data with an artificial neural network. IEEE Trans. Geosci. Remote Sens. 48 (4), 2170–2178.

Zaksek, Klemen, Ostir, Kristof, 2012. Downscaling land surface temperature for urban heat island diurnal cycle analysis. Remote Sens. Environ. 117, 114–124.

Zhan, Wenfeng, Chen, Yunhao, Zhou, Ji, Wang, Jenfei, Liu, Wenyu, Voogt, James, Zhu, Xiaolin, Quan, Jinling, Li, Jing, 2013. Disaggregation of remotely sensed land surface temperature: Literature survey, taxonomy, issues and caveats. Remote Sen. Environ. 131, 119–139.